Publications of the Astronomical Society of the Pacific, 131:114503 (16pp), 2019 November https://doi.org/10.1088/1538-3873/ab33c0

The "Terrascope": On the Possibility of Using the Earth as an Atmospheric Lens

David Kipping
550 W 120th Street, New York, NY 10027, USA; dkipping@astro.columbia.edu
Received 2019 April 5; accepted 2019 July 18; published 2019 October 4

Abstract

Distant starlight passing through Earth's atmosphere is refracted by an angle of just over one degree near the surface. This focuses light onto a focal line starting at an inner (and chromatic) boundary out to infinity, offering an opportunity for pronounced lensing. It is shown here that the focal line commences at ∼85% of the Earth–Moon separation, thus placing an orbiting detector between here and one Hill radius could exploit this refractive lens. Analytic estimates are derived for a source directly behind Earth (i.e., on-axis) showing that starlight is lensed into a thin circular ring of thickness, $WH_{\triangle}/R$, yielding an amplification of $8H_{\triangle}/W$, where $H_{\triangle}$ is Earth's refractive scale height, R is its geopotential radius, and W is the detector diameter. These estimates are verified through numerical ray-tracing experiments from optical to 30 μm light with standard atmospheric models. The numerical experiments are extended to include extinction from both a clear atmosphere and one with clouds. It is found that a detector at one Hill radius is least affected by extinction, as lensed rays travel no deeper than 13.7 km, within the statosphere and above most clouds. Including extinction, a 1-m Hill radius "terrascope" is calculated to produce an amplification of ∼45,000 for a lensing timescale of ∼20 hr. In practice, the amplification is likely halved to avoid daylight scattering i.e., 22,500 (Δmag = 10.9) for $W = 1$ m, or equivalent to a 150 m optical/infrared telescope.

Key words: atmospheric effects

Online material: color figures

1. Introduction

Astronomers crave photons. Simple Poisson counting statistics dictate that the signal-to-noise (S/N) of any astronomical observation relying on electromagnetic waves is proportional to the square root of the number of photons received per unit time. Because the received photon rate is proportional to a telescope's area, then S/N generally scales with telescope diameter. Additionally, a larger telescope offers improved angular resolution, which is is inversely proportional to the diameter.

These two benefits therefore both scale approximately linearly with telescope diameter, yet the cost scales—at best—quadratically (van Belle et al. 2004). Besides the cost of the mirror itself, monolithic mirrors larger than 5 m become difficult to build, due to large structures needed to support them. Segmented designs have therefore been proposed for our largest planned telescopes, such as the 25 m GMT, the 30 m TMT and the 39 m ELT. With GMT priced at $1B and the TMT at $2B, "post-1980" scaling (van Belle et al. 2004) implies that a 100 m telescope would cost ∼$35B, which greatly exceeds the combined 2018 budget of NASA and NSF. A similar situation is true for space-based observatories, where the ∼$10B 6.5 m the *James Webb Space Telescope* (*JWST*) provides an example of how the funding prospects of yet larger telescopes look questionable—a point described as a "crisis in astrophysics" (Elvis 2016).

Faced with the prospect of a stall in our continuously improving view of the universe, it is timely to ask whether there exist any "shortcuts" to catching photons—ways of amplifying the signal without building ever larger structures. Angular resolution can certainly be improved using an interferometric array of small telescopes rather than a single giant structure (Monnier 2003). Photon counts are much more challenging to greatly increase, because the flux count per unit area is defined by an astronomical source's magnitude, implying the only way to collect more photons is to have a larger aperture. If we are unable to build such giant apertures due to their prohibitive cost, the next best thing is to ask if there exists any naturally occurring giant lenses that could serve our purpose?

One example of a natural lens is the Sun. Gravitational deflection and lensing of light by massive objects was predicted by Einstein (1916) and observed for the Sun nearly a century ago (Eddington 1919). von Eshleman (1979) proposed that this lensing could be used for interstellar communication, with subsequent studies considering using the lens for astronomical observations (Kraus 1986; Heidmann & Maccone 1994). Starlight would be focused along a line starting at 550 au and

thus an observatory would need to orbit the Sun beyond this separation, where it would enjoy enormous amplification of distant sources. Besides launch operations, there are challenges with such a mission. It has been argued that interference from the solar atmospheric plasma and limited source selection would pose major challenges to realizing such a proposal (Turyshev & Andersson 2003).

When faced with the prospect of flying to 550 au to exploit an astrophysical lens, it is natural to ask whether there are any alternative astrophysical lenses closer to home? Earth clearly cannot serve as a practical gravitational lens given its relatively low mass, but it does bend light using another physical effect—refraction. A setting Sun is a little more than half a degree lower than it appears as a result of this effect. It therefore stands to reason that a optical ray passing through Earth's atmosphere, skimming above the surface, and then emerging out the other side will refract by just over one degree. Thus, one might imagine an observer at or beyond a distance of $\sim R \cot 1^\circ \simeq 360{,}000$ km (approximately the Earth–Moon separation) would be able to exploit Earth as a refractive lens —a concept referred to as the "terrascope" in what follows. Much like the gravitational lens, this distance is the inner point of a focal line, along which high amplification should be expected.

Refraction through Earth's atmosphere to approximately one lunar separation has been known since the 18th century (Cassini 1740), through studies of the lunar eclipse. This work aims to provide the first quantitative grounding for the terrascope concept by calculating the amplification expected, lens properties, image shapes, lensing timescale, and the effects of extinction. As an initial quantification of these effects, the goal here is not to perform the most realistic calculation possible, but rather estimate the approximate effects that might be expected. Other effects not modeled, such as airglow, pointing stability, and turbulence are briefly explored in the discussion.

The paper is organized as follows. In Section 2 a numerical scheme for calculating refraction is described, as well as a simplified atmospheric model. In Section 3, ray-tracing simulations are described, detailing how lensing solutions may be solved for. In Section 4, the simulations are used to compute the amplification expected for the terrascope as a function of wavelength, observatory distance, and detector diameter. This section also describes estimates for extinction effects such as scattering and clouds. Section 5 concludes by describing ignored effects and practical considerations.

2. Modeling Atmospheric Refraction

2.1. Lensing Through a 1D Static Atmosphere

Consider a luminous source located at a large distance from Earth such that it can be approximated as a point source (we leave consideration of diffuse sources of emission to future work). Light from the source arrives at Earth as an approximately plane-parallel wave with a wavelength λ and can be represented by a sum of parallel rays, each with an impact parameter b (see Figure 1). Earth's atmosphere is considered to be described by a 1D temperature–pressure (TP) profile and is unchanging in time. Earth's atmosphere is then split up into a series of N shells, within which the temperature, pressure, and refractivity is assumed to be constant.

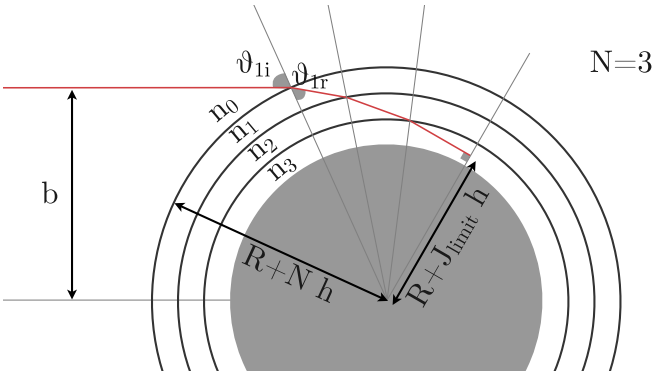

Figure 1. Schematic of a $N = 3$ shell atmosphere where (exagerrated) refraction is calculated by considering the interactions at each shell boundary. (A color version of this figure is available in the online journal.)

The total geopotential altitude of the atmosphere is defined as Z, such that each shell has a thickness of $h = Z/N$ and a refraction index of n_j. Shell indices are assigned in ascending order, such that the deepest layer have the highest index. The outer shell, shell $j = 0$, effectively extends out to infinity and has a refraction index of $n_0 = 1$.

When the ray of light reaches the boundary between from shell $j - 1$ to j, the change in atmospheric density leads to a change in the light's speed and thus refraction occurs as described by Snell's law:

$$n_{j-1} \sin \theta_{i,j} = n_j \sin \theta_{r,j}, \tag{1}$$

where the indices i and r refer to "incidence" and "refraction," respectively. The deflection angle of the ray is therefore

$$\alpha_j = \theta_{i,j} - \theta_{r,j}. \tag{2}$$

At the boundary of $j = 1$ shell, the angle of incidence can be written in terms of the impact parameter, b, by the trigonometric relation

$$\sin \theta_{i,1} = \frac{b}{1} \frac{1}{R + Nh} \tag{3}$$

and thus via Snell's law, we also have

$$\sin \theta_{r,1} = \frac{b}{n_1} \frac{1}{R + Nh}. \tag{4}$$

The angle of incidence at the boundary of the $j = 2$ shell can be deduced from this result, by applying the sine rule inside the triangle subtended from the $j = 1$ boundary intersection to the

$j = 2$ boundary intersection to Earth's center:

$$\sin\theta_{i,2} = \frac{R+Nh}{R+(N-1)h}\sin\theta_{r,1}, \\ = \frac{b}{n_1}\frac{1}{R+(N-1)j} \quad (5)$$

And again, using Snell's law, this gives

$$\sin\theta_{r,2} = \frac{b}{n_2}\frac{1}{R+(N-1)j}. \quad (6)$$

Continuing this process, it is easy to show that

$$\sin\theta_{i,j} = \frac{b}{n_{j-1}}\frac{1}{R+(N-j+1)h}. \quad (7)$$

and

$$\sin\theta_{r,j} = \frac{b}{n_j}\frac{1}{R+(N-j+1)h}. \quad (8)$$

Using Equations (7) and (8) with Equation (2) allows one to calculate the deflection angle at each shell boundary. In practice, this is done by using the sine addition rule

$$\sin\alpha_j = \sin(\theta_{i,j}-\theta_{r,j}), \\ = \sin\theta_{i,j}\cos\theta_{r,j} - \sin\theta_{i,j}\cos\theta_{i,j}, \\ = \sin\theta_{i,j}\sqrt{1-\sin^2\theta_{r,j}} - \sin\theta_{i,j}\sqrt{1-\sin^2\theta_{i,j}} \quad (9)$$

such that

$$\alpha_j = \sin^{-1}\left[\frac{b}{n_{j-1}}\frac{1}{R+(N-j+1)h}\right. \\ \sqrt{1-\left(\frac{b}{n_j}\frac{1}{R+(N-j+1)h}\right)^2} \\ \left. - \frac{b}{n_j}\frac{1}{R+(N-j+1)h}\right. \\ \left.\sqrt{1-\left(\frac{b}{n_{j-1}}\frac{1}{R+(N-j+1)h}\right)^2}\right]. \quad (10)$$

2.2. Critical Refraction Limits

If the impact parameter is low enough, the ray will eventually strike the planetary surface and thus end its journey. Consider the critical case of this such that the ray just grazes the planetary surface tangentially, initiated from an impact parameter $b_{\rm crit}$. If this happens, then it follows that the ray must also reach the deepest atmospheric shell. In that shell, one can draw a right-angled triangle from the planet's center to the two intersection points and write that

$$\sin\theta_{r,N} = \frac{R}{R+h} \quad (11)$$

Now, substituting in Equation (8), we have

$$\frac{b_{\rm crit}}{n_N}\frac{1}{R+h} = \frac{R}{R+h}, \quad (12)$$

which may be solved to give

$$b_{\rm crit} \equiv Rn_N. \quad (13)$$

If the impact parameter is in the range $b_{\rm crit} < b < R+Nh$, then the ray will penetrate Earth's outer atmospheric shell and continue down to some depth before making its way back out of the atmosphere again. Let us write that the deepest shell is given by the index $J_{\rm limit}$. To calculate the total deflection angle, Δ, of a ray, we must calculate $J_{\rm limit}$, because $\Delta = \sum_{j=1}^{J_{\rm limit}}\alpha_j$.

This may be calculated by considering that the cos $\theta_{i,j}$ term in the Δ calculation must be real. The term becomes imaginary if sin $\theta_{i,j} > 1$. Using Equation (7), one sees that this corresponds to

$$\frac{1}{n_{j-1}}\frac{b}{R+(N-j+1)h} > 1. \quad (14)$$

Therefore, one may find $J_{\rm limit}$ by sequentially calculating the above inequality from $j = 1$ up until the condition holds true. At this point, the previous shell is assigned as $J_{\rm limit}$. The total deflection angle, from the lowest altitude to space (space-to-space is simply twice as much) is then computed as

$$\Delta = 2\sum_{j=1}^{J_{\rm limit}}\alpha_j. \quad (15)$$

2.3. Airmass

Aside from computing the deflection angle and deepest shell layer of an incoming ray, one can also compute the airmass traversed, X. The path length can be found by using the sine rule inside the triangles formed between the planet's center and the shell intersection points:

$$d_j = \left(\frac{\sin(\theta_{i,j+1}-\theta_{r,j})}{\sin\theta_{i,j+1}}\right)(R+(N-j+1)h). \quad (16)$$

Substituting Equations (7) and (8) into Equation (16), and after simplification, yields

$$d_j = \sqrt{(R+(N-j+1)h)^2-(b/n_j)^2} \\ - \sqrt{(R+(N-j)h)^2-(b/n_j)^2}. \quad (17)$$

The airmass passed through by a ray is proportional to the path length multiplied by the density. Using the ideal gas law, the density is proportional to pressure over temperature (P/T). Accordingly, airmass is given by

$$X = \frac{\sum_{j=1}^{J_{\rm limit}} d_j P_j/T_j}{X_0}, \quad (18)$$

where X_0 is a constant of proportionality defined such that $X = 1$ for a ray which travels from sea level to space along the zenith. This equates to

$$X_0 \equiv \sum_{j=1}^{N} hP_j/T_j. \tag{19}$$

2.4. Model Atmosphere

As stated earlier, this work assumes that within a given shell, the pressure, temperature, and refractivity are constant. In other words, a 1D static atmosphere. The purpose of this work is to simply demonstrate the concept of the terrascope. If worthwhile, future work could be undertaken to use more sophisticated atmospheric models accounting for weather, turbulence, and regional differences. For now, the goal is merely to compute the approximate feasibility and properties of the terrascope, by making reasonable but ultimately simplifying assumptions.

To accomplish this, the US Standard Atmosphere 1976 (National Geophysical Data Center 1992) was adopted as a fiducial TP profile. This atmosphere can be considered to be an average over the global climate but can be a poor representation for particular local climates. To investigate the impact of differing conditions, five other standard TP profiles were utilized—in particular the same atmospheres as used by `lowtran7` (Kneizys et al. 1988). These are the "tropical," "mid-latitude summer," "mid-latitude winter," "sub-arctic summer" and "sub-arctic winter" models (these are shown in Figure 2).

The models define a continuous TP profile from 0 to 85 km geopotential altitude (z) but with functional changes occurring at six key boundaries distributed in altitude. Within each of the layers (defined by sharp boundaries), the lapse rate, $\mathbb{L}$, is varied, and the pressure computed assuming an ideal gas and vertical pressure variation of $dP/dz = -\rho g$ (where ρ is the density of air and g is the acceleration due to gravity).

Temperature, as a function of geopotential altitude, within the kth layer is defined by

$$T_k[a] = T_{k-1} + \mathbb{L}_k(z - z_k), \tag{20}$$

where T_0 is the temperature at sea level. The pressure is then given by

$$P_k[z] = \begin{cases} P_{k-1}\exp\left(-\dfrac{-g_0 M(z - z_k)}{RT_{k-1}}\right) & \text{if } \mathbb{L}_k = 0, \\ P_{k-1}\left(\dfrac{T_{k-1}}{T_k[z]}\right)^{\frac{g_0 M}{R\mathbb{L}_k}} & \text{otherwise,} \end{cases} \tag{21}$$

where P_0 is the pressure at sea level and $g_0 M/R = 34.1645\ \mathrm{K\,km^{-1}}$.

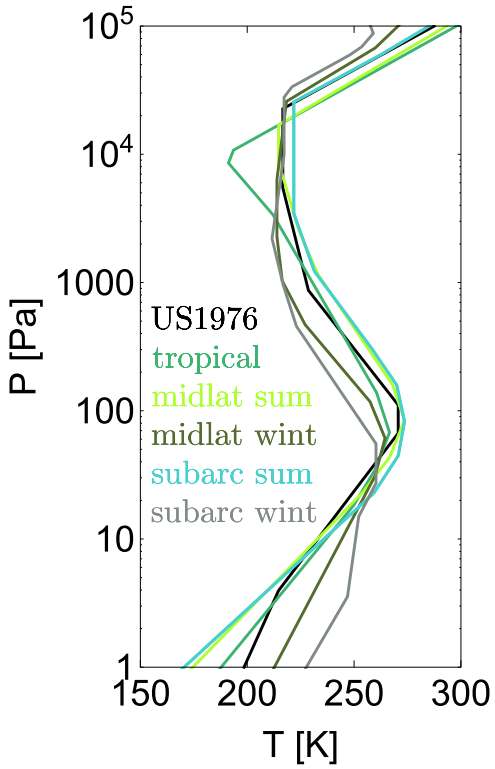

Figure 2. Temperature–pressure profiles for six standard atmospheres used in this work.

2.5. Calculating Refractivity

The refractivity of air, η, equals the refraction index, n, minus unity. Given a shell's pressure and temperature defined by the US Standard Atmosphere 1976, the refractivity may be computed using a semi-empirical formula. In this work, the expression of Birch & Downs (1994) is adopted because the expression is found to be in better agreement with recent measurements than the Edlén (1994) formula, largely due to the increase in ambient carbon dioxide levels (Birch & Downs 1994). The refractivity of dry air is thus given by

$$\eta = 10^{-8}P\left(C_1 + \frac{C_2}{C_3 - \sigma^2} + \frac{C_4}{C_5 - \sigma^2}\right)\left(\frac{1 + 10^{-10}P(C_6 - C_7T')}{C_8(1 + C_9T')}\right), \tag{22}$$

where T' is the temperature in Celsius, σ is the reciprocal of the wavelength of light in a vacuum in units of nanometers, and C_1 to C_9 are constants.

The calculations described throughout the rest of the paper were also repeated using moist air refractivity, instead of dry air, using the appropriate correction (Birch & Downs 1994). However, this was found to produce very minor changes to the

results and thus the dry air formula will be used in what follows.

It is instructive to consider the approximate relationship as well. Refractivity is proportional to the gas density. For an isothermal atmosphere, one expects $\rho \propto e^{-z/H}$, where H is the scale height and z is the altitude. Accordingly, one expects $\eta \propto e^{-z/H}$ too.

3. Ray-tracing Simulations

3.1. Generating a Training Set

Two physical principles are critical in consideration of the terrascope, refraction, and extinction. The issue of atmospheric extinction will be tackled later in Section 4.3, thus we first deal with refraction using the expressions found earlier in Section 2 to ray trace through Earth's atmosphere. In what follows, rays are only traced from space to the point of closest approach to the Earth's surface. Because the assumed model atmosphere is static and 1D , the egress path will be identical to the ingress path and one may exploit this symmetry to save computational effort.

Before a ray can be traced, it is first necessary to choose how many shells (N) will be used for ray-tracing experiment. In general, the greater the number of shells, the more accurate the integration, but at greater computational expense. Further, it is necessary to choose up to what geopotential altitude the atmosphere terminates, Z (technically the atmosphere extends to infinity but this of course is not computationally reasonable, nor are the standard atmospheres well-defined above 86 km).

In preliminary ray-tracing experiments, it was noted the deflection angles follow a generally smooth trend with respect to impact parameter until the impact parameter approaches R +86 km. At the 86 km boundary, the refractivity is discontinuous, jumping off a monotonically decreasing smooth function down zero. This appears to introduce peculiar behavior for extreme impact parameters and thus $Z = 80$ km was adopted in an effort to avoid this regime. A high but computationally efficient resolution was chosen such that each shell has a thickness of $h = 10$ cm, corresponding to 800,000 steps.

Let us choose a particular wavelength, λ, of light to work with. Using this wavelength, one still needs to choose an impact parameter, b, before ray tracing can be executed. To generate a suite of examples, let us define a grid of impact parameters varying from R to $R + Z$ uniformly spaced in geopotential altitude. Because the numerical resolution of the atmosphere is itself 800,000, the resolution used for b cannot be higher than this and a reasonable choice is to adopt an order-of-magnitude lower to ensure the highest possible scan yet retain reliable results. Accordingly, a resolution in b of 80,000 was adopted (i.e., 1-m step sizes).

These experiments essentially generate a training set from which one can learn the relationship between b and deflection angle, Δ (as well as other properties). However, the set is conditioned upon a specific choice of λ. To build a complete training set, it is necessary to also vary λ. This is done by creating a grid from $\lambda = 0.2$ to $30\,\mu$m with 219 examples spaced log-uniformly. This wavelength range corresponds to the range of support for the `lowtran7` extinction model that will be used later (see Section 4.3).

In each run, the total deflection angle, Δ, is recorded, as well as the minimum geopotential height achieved by the ray[1] ("depth"), D, and the airmass traversed through, X. It was found that impact parameters close to the 80 km boundary exhibited slight trend differences than the bulk, suggestive of a numerical error. To alleviate this, samples with $b > 77$ km were excluded, as well as samples for which the ray strikes Earth, leaving a total of 10,606,382 ray-tracing experiments that were saved.

3.2. Interpolation Scheme

To generalize the numerical results to arbitrary values of b and λ, one can apply interpolation to the training data.

3.2.1. Critical Impact Parameter, b_{crit}

For each ray-tracing experiment, only X, D and Δ are saved and so these are the three terms that require interpolation. However, a useful product of these is $b_{\rm crit}$, the impact parameter at which $D = R$. Because the simulations iterate through in 1-m steps in b, one may simply cycle through the list until $D < R$ and save the previous example as $b_{\rm crit}$, which will have a maximum associated error of 1 m.

In total, there are 220 training examples of $b_{\rm crit}$ versus λ. When cast as $b_{\rm crit}$ against λ^{-2}, the relationship appears quasi-linear, thus it is using this parameterization that the interpolation is performed. Because the number of samples is relatively small, it is feasible to perform Gaussian process (GP) regression (Michael 1999; Rasmussen & Williams 2006), in this case using a squared exponential kernel. Using exhaustive leave 1-out, this process is repeated to evaluate the error in the final estimates. The final interpolative function, shown in Figure 3, has a maximal error of one meter, which is the numerical error of the training set to begin with. It therefore represents an excellent predictor and is adopted in what follows.

3.2.2. Airmass, X, and Depth, D

For airmass and depth, a GP regression is impractical due to the much larger and 2D training set of over 10 million samples. Instead, this large sample is suitable for a dense interpolative net. As with $b_{\rm crit}$, it was found that λ^{-2} provides a more linear basis for training for both X and D. The 2D bilinear

[1] In this way, b and D are closely related; b is the minimum separation between Earth's center and the ray in the absence of refraction, whereas D is the same but with refraction turned on.

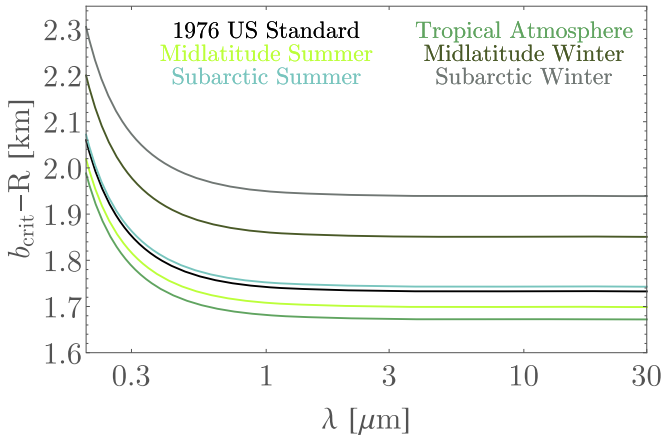

Figure 3. Critical impact parameter as a function of wavelength. Impact parameters below this will refract so much they strike Earth. The different lines shows the effect of varying the climate model.

interpolation therefore maps $\{\lambda^{-2}, b\} \rightarrow X$ and D. Examples of the interpolative function are shown in Figure 4.

To provide further intuition and context, we also show the "effective" refractivity of Earth's atmosphere in Figure 4. This is computed by taking the computed deflection angles and solving for the equivalent refractivity needed for that deflection using a single-layer atmosphere.

Using leave 1-out, one may evaluate the error of these interpolations. This is done by leaving a random example out, re-training the interpolation, and then evaluating the residual between the omitted sample and the interpolated prediction of said point. Because the training is relatively expensive computationally, the aforementioned Monte Carlo experiment is limited to 1000 realizations.

This process revealed the bilinear scheme is able to perform excellent interpolation across the grid. The relative airmass residuals show a non-Gaussian distribution with a standard deviation of 0.68%, a mean absolute error of 0.13% and a 99.9% of samples exhibiting an absolute error less than 0.11%. For depth, the standard deviation of the absolute residuals is 0.030 m, the mean absolute error is 0.012 m, and 99.9% of samples have an absolute error less than 0.20 m.

3.2.3. Deflection Angle, Δ

For deflection angle, it was found that simple bilinear interpolation did not provide particularly stable results, too closely tracing out the small numerical errors found in the simulations rather than smoothing over them. Another problem with this scheme was that as the simulations approach $b \rightarrow b_{\rm crit}$, there is no training data for deflection angle because it cannot be defined below this point. This led to unstable extrapolations in the final shell.

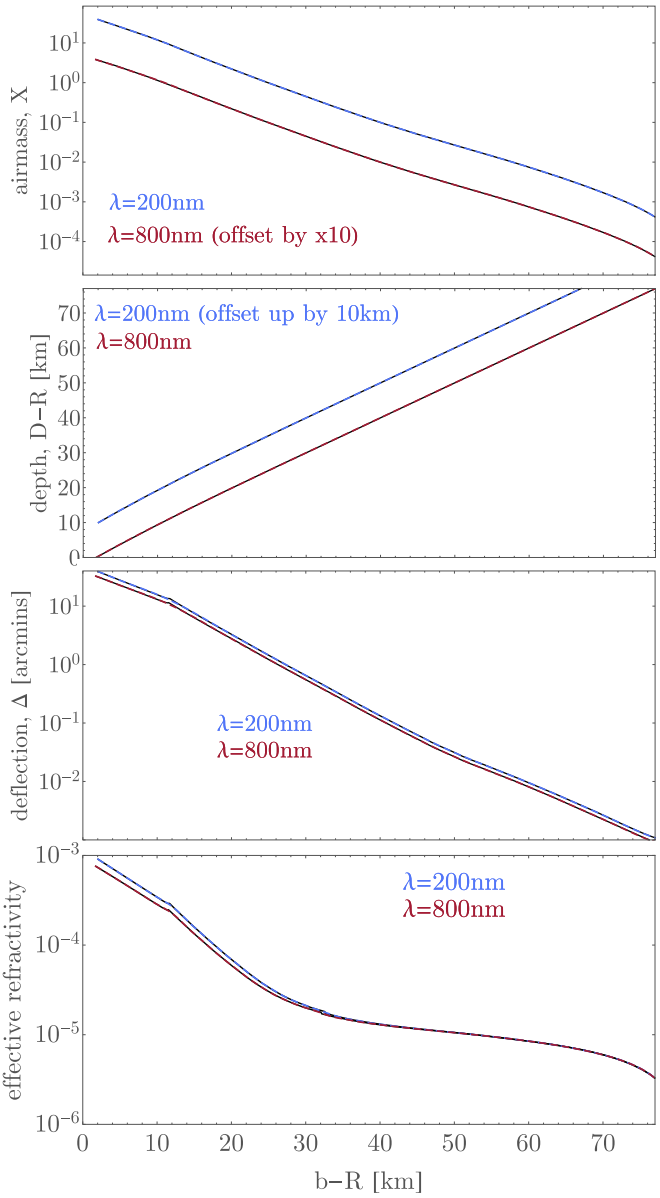

Figure 4. Simulation results are shown in dark gray, interpolative functions in dashed colors. Upper: airmass traversed for a ray traveling through Earth's atmosphere from space to its closest approach to Earth as function of impact parameter. Middle-upper: depth of the ray at closest approach. Middle-lower: deflection angle of the ray by the time it reaches closest approach (rays interior to the critical impact parameter are omitted). Lower: "effective" refractivity of the atmosphere, calculated as described in the main text.
(A color version of this figure is available in the online journal.)

Instead of bilinear interpolation, a GP with a rational quadratic kernel is trained on each wavelength slice independently. The training data is also thinned by a factor of 100 to expedite the training (leaving approximately 750 samples per slice). Rather than use Δ as the target function, we use $\log \Delta$ which behaves quasi-linearly with respect to $(b - R)$, the

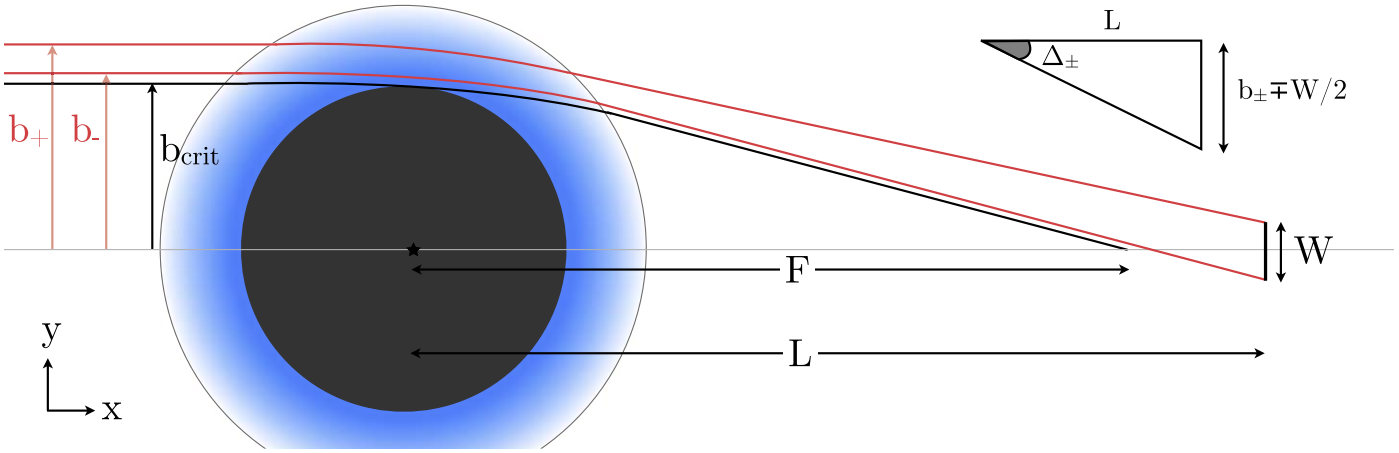

Figure 5. Illustration of a detector of diameter W utilizing the terrascope. Two rays of different impact parameters, but the same wavelength, lens through the atmosphere and strike the detector. The ring formed by those two rays enables a calculation of the amplification. In this setup, the detector is precisely on-axis. (A color version of this figure is available in the online journal.)

independent variable for the training. The GP is used because it smooths over the numerical noise introduced by our machine-precision calculations.

Calling the GP predictor is computationally slow, and so a library of predictions is generated for later use. This library samples the original simulations at a thinning rate of ten along the b-axis, giving 7506 samples. The library is then interpolated using splines in cases where needs to evaluate the deflection angle at intermediate choices of Δ. Comparing to the original samples, the agreement of the final interpolations is better than 1.9% for all samples, with a standard deviation of 0.83%. The interpolated function is shown in Figure 4.

3.3. Computing on-axis Amplification

Amplification is defined here as the intensity received by a detector using the terrascope relative to the intensity the same detector would receive in the absence of Earth . The latter of these two terms is simply the incident flux multiplied by the collecting area of the detector, $\pi(W/2)^2$, where W is the diameter/aperture of the detector. In the same way, the intensity received by the terrascope can be computed by simply considering the effective light-collecting area. In what follows, it is assumed that the source, the lens, and the detector are all perfectly aligned, which is referred to as "on-axis."

The setup is illustrated in Figure 5. A ray of wavelength λ and impact parameter of b_- is refracted by an angle Δ_- such that it strikes lower tip of the detector located at a distance of L. Another ray with the same wavelength but a higher impact parameter, b_+, is refracted by an angle $\Delta_+ < \Delta_-$ and eventually strikes the upper tip of the detector. It follows that all rays of wavelength λ and impact parameter $b_- \leqslant b \leqslant b+$ will strike the detector. In the on-axis case considered here, along with the assumption of a 1D atmosphere, the problem is symmetric about the x-axis and thus the lensing region is circular ring of area $\pi\ (b_+^2 - b_-^2)$, meaning that the amplification $\mathcal{A}$, is given by

$$\mathcal{A} = \epsilon \frac{b_+^2 - b_-^2}{(W/2)^2}, \tag{23}$$

where ϵ is a loss parameter describing the degree of extinction. Rather than forming a single focus point, light focuses along a line much like the case of gravitational lensing. The maximum distance of the focal line is infinity, but the inner distance is well-defined and it is labeled as F in what follows. This distance corresponds to a ray striking Earth at the critical impact parameter, $b_{\rm crit}$ (for a given wavelength). The focal distance is given by simple trigonometry

$$F = b_{\rm crit} \cot \Delta_{\rm crit} \tag{24}$$

where

$$\Delta_{\rm crit} \equiv \lim_{b \to b_{\rm crit}} \Delta(b). \tag{25}$$

In the wavelength range of 0.2–30 μm, the inner focus point varies from $\simeq$200,000 to $\simeq$350,000 km, depending on the wavelength and climate model (see Figure 6). This indicates that it would be possible to focus light at the lunar distance itself because the focal line extends to infinity past this inner point. Accordingly, observatories at or beyond the lunar distance could be feasible locations for the terrascope detector.

The impact parameters b_+ and b_- dictating the amplification can be derived by geometrical arguments. Consider a ray of impact parameter b_+ which deflects by angle $\Delta[b_+]$ such that it strikes the upper tip of the detector located at a distance L. Because the offset from the x-axis of the upper detector tip is

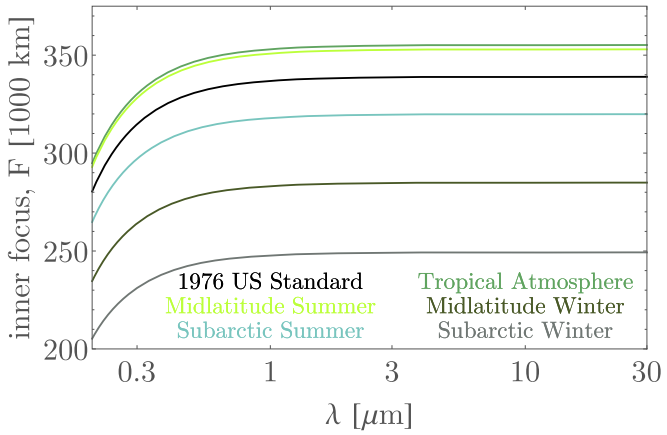

Figure 6. Location of the inner focal point of the terrascope as a function of wavelength. Rays cannot focus interior to this point because they would strike Earth's surface. Results shown for six different model temperature–pressure profiles.

$W/2$ and thus one can write that

$$b_+ - L\tan\Delta[b_+] = W/2. \tag{26}$$

Similarly, consider a ray which passes a little deeper through the planetary atmosphere at impact parameter b_-, such that it deflects enough to strike the lower tip of the detector, which satisfies

$$b_- - L\tan\Delta[b_+] = -W/2. \tag{27}$$

In practice, solutions for these two impact parameters are found through a numerical Nelder–Mead optimizer, because of the subtle dependency of Δ upon b (see Section 3.2).

This optimization is repeated for various choices of L, W and λ. For λ, the original grid of 220 wavelengths was adopted. For L, it was found that the inner focus of the shortest wavelength with the US Standard Atmosphere 1976 model was 281,700 km and thus a uniform grid was adopted from this distance out to 1,500,000 km (the Hill sphere of Earth) with 101 steps. Finally, for W, five fiducial diameters are adopted: 10^{-2}, 10^{-1}, 10^{0}, 10^{1} and 10^{2} m.

3.4. Analytic Estimates

Although the numerical experiments provide the most precise view, it is instructive to consider the approximate scaling relations expected. One can note that the Δ function is approximately log-linear and thus can be approximated as $\Delta \simeq \Delta_0 e^{-(b-R)/H_\Delta}$ where H_Δ is an effective scale height for the lensing, equal to 6.911 km to within three-decimal places for all rays between $\lambda = 0.2\,\mu$m to $\lambda = 30\,\mu$m. Using this approximate formalism, Equations (26) and (27) can be combined to give

$$W = \Delta b \; + L(\tan(\Delta_0 e^{-(b_- - R)/H_\Delta}) - \tan(\Delta_0 e^{-(b_+ - R)/H_\Delta})) \tag{28}$$

where $\Delta b = (b_+ - b_-)$. Taking a small-angle approximation, replacing $b_- = b_{\rm mid} - \Delta b/2$ and $b_+ = b_{\rm mid} + \Delta b/2$, and then Taylor expanding for small $\Delta\, b$ (thin ring approximation) gives

$$\Delta b\left(1 + \frac{L}{H_\Delta}\Delta_0 e^{-\frac{b_{\rm mid}-R}{H_\Delta}}\right) = W. \tag{29}$$

To reach the detector, one may write that $\Delta \simeq b/L$, or simply $\Delta \sim R/L$ by noting that $R \gg (b - R)$. This allows us to write that

$$\begin{aligned}\Delta b &\sim \frac{W}{1 + (L/H_\Delta)(R/L)},\\ &\sim \frac{W}{(R/H_\Delta)},\end{aligned} \tag{30}$$

where the second lines has used the fact $R \gg H_\Delta$. While one might naively intuit that $\Delta b \sim W$, the gradient in the refractive index means the rays needs to be closer together than this, as even a slight angular difference is magnified over the large distance L. The denominator is of order 10^3 and thus implies that for a 1-m diameter detector, the lensing ring is about a millimeter thick.

The above allows one to approximately estimate the amplification, $\mathcal{A}$. If one writes that $b_+ = b_- + \Delta b$, then Equation (23) becomes $\mathcal{A} = \epsilon b_-^2\left(\left(1 + \frac{\Delta b}{b_-}\right)^2 - 1\right)\Big/(W/2)^2$. Because $\Delta b \ll W$ and $b_- \sim R$, then provided $W \ll R$ (which practically speaking will always be true), one may write that $\frac{\Delta b}{b_-} \ll 1$. This permits a Taylor expansion of $\mathcal{A}$ such that

$$\mathcal{A} \simeq 2\epsilon b_- \Delta b/(W/2)^2 \tag{31}$$

which can be further refined by adopting $b_- \sim R$ and using Equation (30) to write

$$\begin{aligned}\mathcal{A} &\sim 2\epsilon R\frac{W}{(R/H_\Delta)}\left(\frac{4}{W^2}\right),\\ &\sim 8\epsilon H_\Delta/W.\end{aligned} \tag{32}$$

Because $H_\Delta = 6.911$ km, then $\mathcal{A}/\epsilon \sim 55{,}000/W$, which gives a first estimate for the approximate degree of amplification expected. The effective aperture size is given by $\sqrt{\mathcal{A}}$ and thus equals $W_{\rm eff} \sim 235\epsilon^{1/2}\sqrt{W/(\rm m)}$ m.

3.5. Computing Off-axis Amplification

The alignment of the source, lens, and detector is instantaneous. While useful for estimating the limiting amplification, practically speaking the source spends infinitesimal time at this position and so the useful lensing time is defined by the off-axis positions. Amplification still occurs off-

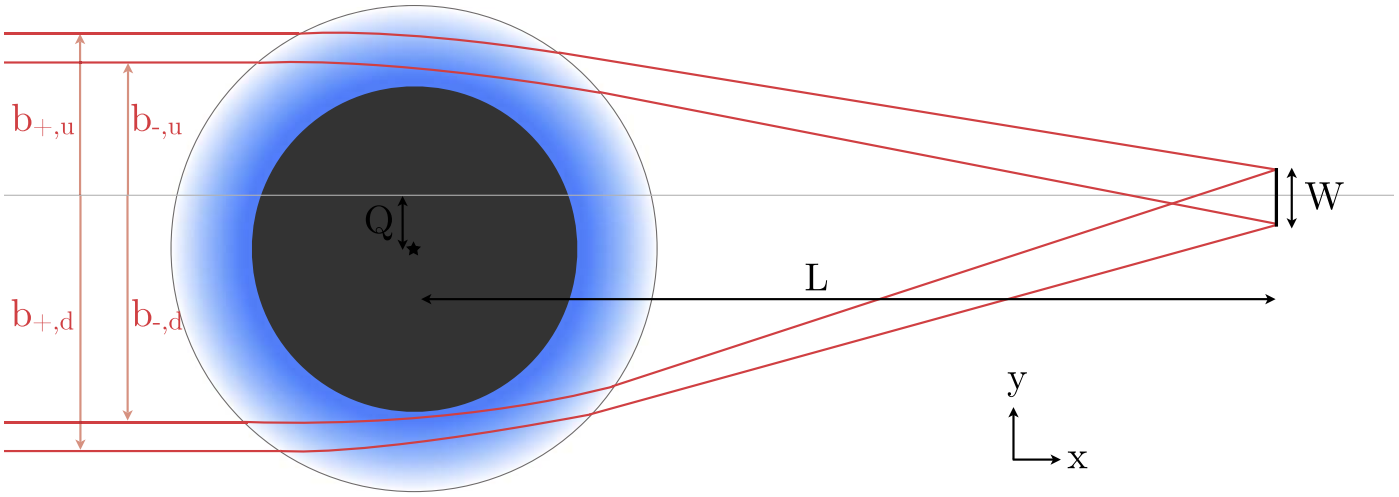

Figure 7. Same as Figure 5, except for off-axis lensing. Only the extrema rays in the $z = 0$ plane are shown.
(A color version of this figure is available in the online journal.)

axis but now the rays which reach the detector must be deflected by different angles, depending upon whether the rays travel above or below the mid-plane.

Consider that Earth is offset from the line connecting the source and the detector's mid-point by a distance Q, as shown in Figure 7. Although in reality Earth is 3D and rays can take different paths than the four lines shown in this diagram, the four rays represent the most extreme affected paths as a result of the translation shift. All four rays can reach the detector provided the following four conditions hold true:

$$\begin{aligned} L\tan\Delta[b_{-,d}] - b_{-,d} &= +W/2 + Q, \\ L\tan\Delta[b_{+,d}] - b_{+,d} &= -W/2 + Q, \\ L\tan\Delta[b_{-,u}] - b_{-,u} &= +W/2 - Q, \\ L\tan\Delta[b_{+,u}] - b_{+,u} &= -W/2 - Q. \end{aligned} \tag{33}$$

Or more generally, received rays satisfy

$$\begin{aligned} L\tan\Delta[b_d] - b_d - Q &\leqslant |W/2|, \\ L\tan\Delta[b_u] - b_u + Q &\leqslant |W/2|. \end{aligned} \tag{34}$$

Naturally, if $Q \gtrsim (R + Z)$, then no deflection is required and rays will arrive at the detector unlensed above the detector axis.

Consider a ray that now lives out of the plane, with a $\hat{z}$-axis offset of $\beta_{d,z}$. For a ray below the $\hat{x}$-axis, the incident ray has a detection axis offset in the $\hat{y}$-direction of $\beta_{d,y} + x$, which when combined with the z term gives a Euclidean offset from the detector axis of $\beta_d = \sqrt{(\beta_{d,y} + Q)^2 + \beta_{d,z}^2}$ but an impact factor from the planet of $b_d = \sqrt{\beta_{d,y}^2 + \beta_{d,z}^2}$. One may write that $\beta_{d,y} = b_d \cos\phi$ and $\beta_{d,z} = b_d \sin\phi$, where ϕ is the azimuthal angle about the $\hat{x}$-axis of the incident ray. Now the total offset from the detector axis is given by $\beta_d = \sqrt{b_d^2 + Q^2 + 2b_d Q\cos\phi}$. Similarly, if the incident ray were above the detector axis, then $\beta_u = \sqrt{b_u^2 + Q^2 - 2b_u Q\cos\phi}$. For a circular detector of radius $W/2$, rays will strike the detector if

$$\begin{aligned} L\tan\Delta[b_d] - \sqrt{b_d^2 + Q^2 + 2b_d Q\cos\phi} &\leqslant |W/2|, \\ L\tan\Delta[b_u] - \sqrt{b_u^2 + Q^2 - 2b_u Q\cos\phi} &\leqslant |W/2|. \end{aligned} \tag{35}$$

If $Q = 0$ in the above (i.e., on-axis), then these expressions are identical to the previous equations in Section 3.3. Also, setting $\phi = 0$ recovers Equation (34). Accordingly, one twists ϕ in the range $-\pi/2 < \phi < \pi/2$ for both expressions and expects them to meet at the extrema (which is indeed true). Moreover, one can generalize the above pair into a single expression where $-\pi/2 < \phi < 3\pi/2$:

$$L\tan\Delta[b] - \sqrt{b^2 + Q^2 + 2bx\cos\phi} \leqslant |W/2|, \tag{36}$$

Unlike the on-axis case, the ring of lensed light no longer forms a circle and more closely resembles an egg-shape, which is illustrated in Figure 8. This occurs because each lensed ray now requires a different deflection angle to reach the detector, as a result of the offset between the source, lens, and detector. This, in turn, means that the lensing depth—which strongly controls the deflection angle (see Figure 4)—is different for each lensed ray. For $Q \ll R$, the shape is essentially circular, for $Q \sim R$ the shape is highly oval, and for $Q \gg R$, up to a maximum critical point, the shape disappears behind the planet.

4. Calculation Results

4.1. Aperture Scaling

For a 1-m diameter telescope, typical nonextincted amplifications are found in the range of 50,000–80,000—using the numerical methods described in Section 3. For a 1-m aperture,

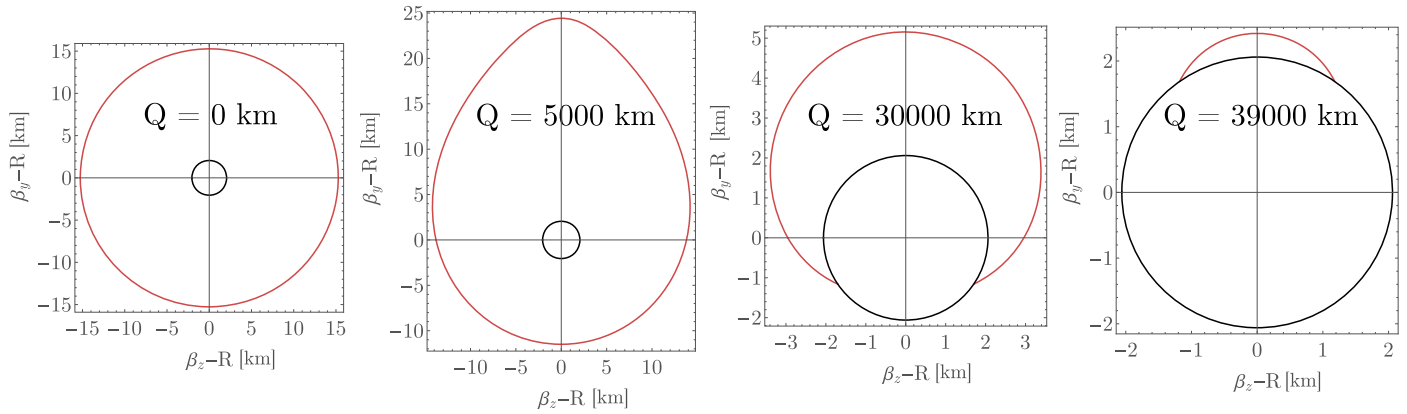

Figure 8. Numerically computed shapes of the lensing strata for three different offsets (red lines).These are the altitudes of the rays above Earth in order for them to come to a focus point at distance L. Black lines show the critical impact parameter inside which rays strike the planet. They represent a kind of refractive surface, below which rays will eventually the intercept the physical surface—which is located at the origin. Calculations use the US Standard Atmosphere 1976, $\lambda = 0.2$ μm and $L = R_{\rm Hill}$. Shapes are exaggerated by virtue of the subtraction of R off both axes.
(A color version of this figure is available in the online journal.)

the lensing ring is just over a millimeter in thickness. For other aperture sizes the thickness is found to scale with the inverse of the aperture diameter (see Figure 9) i.e., $\Delta b = (b_+ - b_-) \propto W$. These numerical results agree with the approximate analytic estimates deduced earlier in Section 3.4.

Changing the telescope aperture has a dramatic impact on the amplification. A clear pattern is that the amplification scales as $1/W$. For example, the amplification of a 10 m detector is 10 times less i.e., 7000–8000. This result was also found in our earlier approximate analytic estimates in Section 3.4. This scaling result indicates that one may simply consider the results for a fixed fiducial detector and scale appropriately. In what follows, $W = 1$ m is adopted and thus the amplification of such an aperture is denoted as $\mathcal{A}_0$.

Taking the amplification and the aperture size used, one can estimate what the effective aperture of the telescope would have to be to match the terrascope. Using the scaling law just described, this allows the effective aperture to be compactly expressed as

$$\left(\frac{W_{\rm eff}}{\rm m}\right) = \sqrt{\mathcal{A}_0 \epsilon \left(\frac{W}{\rm m}\right)} \tag{37}$$

This reveals that the effective aperture of the terrascope equals the actual aperture when $W = \mathcal{A}_0$ meters i.e., ∼80 km, setting an upper limit for the useful size of a terrascope observatory.

4.2. Distance Dependency

Figure 9 shows the amplification as a function of L, illustrating how there is an overall drop-off in amplification away from the inner focus. Although the overall maxima occurs at the inner focus, a curious second maxima occurs at around $L = 500{,}000$ km but appears highly chromatic. These maxima all corresponds to rays with a depth of $\simeq H_\Delta$ revealing their commonality.

Consider fixing L to several plausible options as depicted in Figure 10, which shows the wavelength dependent amplification for a 1-m aperture. The deepest telluric depth of the rays received by the detector is shown in the second panel of that figure, illustrating how redder light needs to travel deeper to reach the observatory. The airmass traversed is shown in the top panel.

In all cases, the rays travel through a substantial amount of airmass and thus one might question whether atmospheric extinction would overwhelm any gains made by the terrascope setup. Two forms of extinction are considered here—clear-sky scattering and interception with clouds. These are dealt with separately in what follows.

4.3. Clear-sky Extinction

To estimate extinction, the `lowtran7` transmittance and radiance package is used (Kneizys et al. 1988). Practically speaking, the code used is a `python` wrapper implementation of `lowtran7` (available at https://github.com/scivision/lowtran), where the `TransmittanceGround2Space.py` script is run setting the zenith angle to 90°. `lowtran7` computes transmittance from the UV/optical out to 30 μm and thus this defines the wavelength range considered inn what follows.

The code is run for 41 choices of observer height, from 0.01 to 100 km in log-uniform steps. The 100 km run is so close to 100% transmittance it is defined as such in what follows to provide a crisp boundary condition for interpolation. Intermediate observer heights are then interpolated as desired using splines.

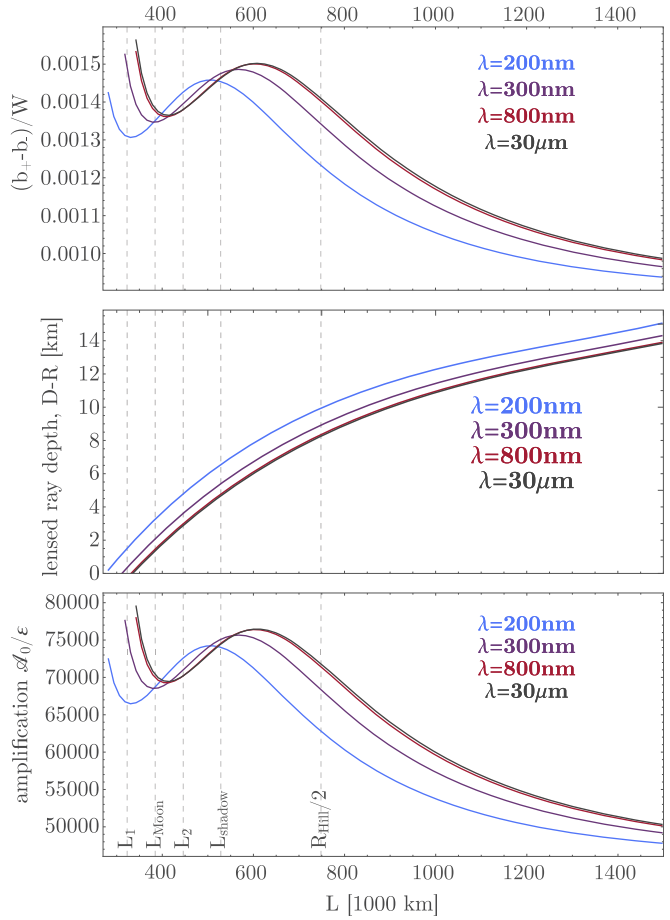

Figure 9. Amplification (lower panel) of 1-m detector using the terrascope as a function of separation from Earth, *L*, for four different wavelengths of light. The upper panel shows the corresponding depth of the ray, and the middle panel shows the lensing ring width.

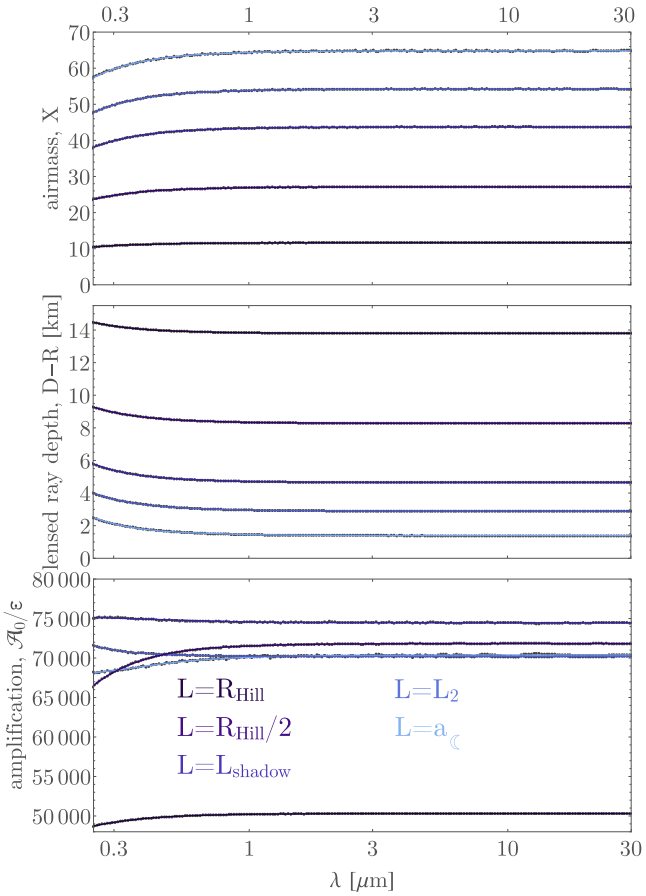

Figure 10. Airmass traversed, telluric depth, and amplification as a function of wavelength for a 1-m telescope at five possible locations.

The amplification after extinction for a given observatory may now be computed. This is done by evaluating the `lowtran7` spectral interpolator at a depth equal to the depth traveled by the lensed rays, which is itself a function of wavelength. Because `lowtran7` assumes ground-to-space (although "ground" here is really just a user-chosen altitude), then space-to-ground-to-space transmission will simply be the self-product. Finally, this function is then multiplied by the chromatic amplification function for the lunar observatory.

As a test of the `lowtran7` model, the transmission was converted to an equivalent atmospheric extinction coefficient for some common optical filters. The extinction coefficient for *B*-band was found to be 0.45, *V*-band 0.28, *R*-band 0.19, *I*-band 0.086, and *H*-band 0.080. These all line-up with typical coefficients for a good observing site.[2]

[2] See http://spiff.rit.edu/classes/phys445/lectures/atmos/atmos.html for a pedagogical description of extinction coefficients and some typical values.

Figure 11 shows the amplification for 1-m terrascope observatory after accounting for the `lowtran7` extinction. Despite the extinction, amplification up to 70,000 remains feasible. One can see from Figure 11 that extinction is severe for detectors at the Moon's orbital radius, because lensed rays need to travel deep through Earth's atmosphere—just a couple of km (see Figure 9). As we move out in orbital radius, sufficient lensing is obtained at higher altitudes thereby reducing the effect of atmosphere extinction, with clear benefits to such detectors.

4.4. Interception by Clouds

The grazing nature of the terrascope lensed rays means that interception by clouds has the potential to dramatically attenuate the overall transmission through the atmosphere. Even wispy high-altitude cirrus clouds, with an optical depth of ∼0.1 and 1 km thickness scale, can appear completely opaque to terrascope rays because the path length can be up to ∼100 km. This simplifies the analysis, because one can simply assume that encountering any kind of cloud leads to zero

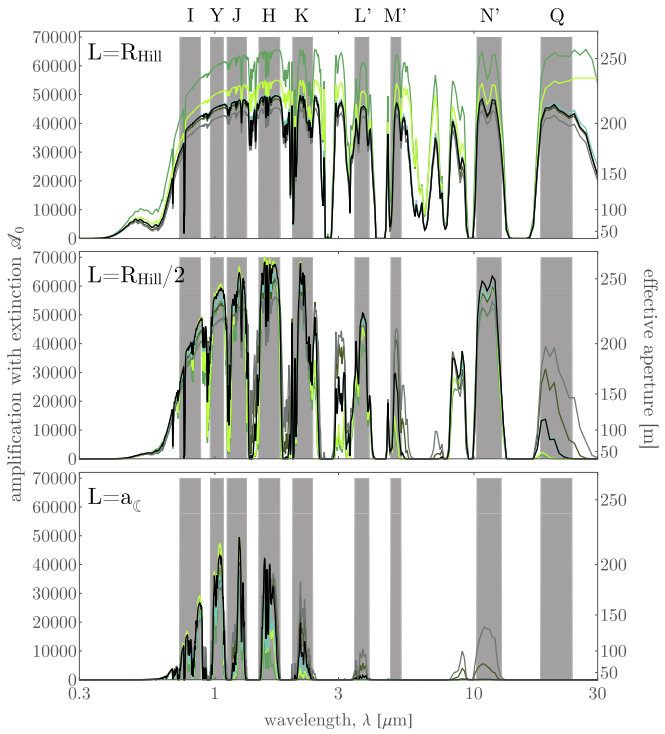

Figure 11. Amplification after extinction expected for a 1-m diameter telescope at Earth's Hill radius (top), half the Hill radius (middle) and the Moon's separation (bottom). Six atmosphere models are shown (same color coding as Figure 6), which control temperature–pressure profiles (and thus refractivity profile) as well as the extinction computed using `lowtran7`. All models assume no clouds. Standard photometric filters highlighted in gray, except for L, M, and N which are slightly offset to encompass the optimal regions.

transmission. The real question is then what is the frequency which rays intercept a cloud?

It is important to recall that for rays lensed onto a Hill sphere terrascope, the deepest altitude penetrated by the ray is 13.7 km (see Figure 10), and at this altitude there are almost no clouds. Thus, if $L \sim F$, then the $(D - R) \sim 0$ and lensed rays will have to traverse not only a large airmass but also most likely intercept opaque clouds during their journey. On the other hand, observatories away from F require less deflection and thus need not travel so deep through Earth's atmosphere, largely avoiding clouds.

The relationship between L and $(D - R)$ is well-constrained from our simulations. The first thing to highlight is that redder than about a micron, the refraction is almost achromatic and thus the lensing depth is approximately constant for a given L (this is apparent from Figure 10). Thus, one can simply take $\lim_{\lambda\to\infty}(D - R)$ as an excellent approximation for wavelengths redder than a micron. The second thing to highlight is that if one varies L from F out to $R_{\rm Hill}$ in 100 uniform steps, the relationship is tight and monotonic, empirically found to be described by

$$\lim_{\lambda\to\infty}(D - R) \simeq a_0(1 - a_1 e^{-L/a_2}), \tag{38}$$

where for the US Standard Atmosphere 1976 model one obtains $a_0 = 15.54$ km $a_1 = 1.829$ and $a_2 = 551{,}100$ km (to four significant figures).

To estimate the effect of clouds, this work uses data from the High-resolution Infrared Radiation Sounder (HIRS) satellite instrument. Statistical properties of clouds have been cataloged with multi-year observations taken from polar orbit and are have been described in the literature (Wylie et al. 1994a, 1994b). This work uses the data made available at http://ftp.ssec.wisc.edu. Within a field of view of approximately 20 km by 20 km, HIRS determines the effective cloud fraction, $N\,\epsilon$, where N is the frequency of clouds and ϵ is the emissivity, which approximately equals one minus the transmission, T.

Averaging over all longitudes, latitudes, and months, the average effective cloud fraction for all clouds below a pressure level of 950 mbar is 76.6%. At or below a pressure level of 200 mbar the effective cloud fraction has dropped to 5.4%. The global averages are shown in Figure 12 where pressure levels have been converted to altitudes. It is found that the nine available data points, for any given location, are well described by a broken power law, with a break at around one scale height (as shown by the smooth function overplotted in the left panel of Figure 12).

To generalize the HIRS data to arbitrary locations and altitudes, the data set is first interpolated to a regularized grid then each location fitted using the broken power law. The interpolation is necessary because no data is available north of 84° latitude or south of −84°. To interpolate, longitudinal great circles are drawn around Earth in one-degree intervals and then the data is wrapped around to ensure a continuous periodic function. A GP with a Mattern-3/2 kernel is trained at each pressure level across all latitudes and used to fill in the missing latitudes. The broken power law is then fitted to each one-square degree location independently, where the free parameters are two slopes, one offset, and one transition point.

To simplify the analysis, only $L > R_{\rm Hill}/2$ is considered in what follows, meaning that $\lim_{\lambda\to\infty}(D - R) > 8.2$ km. At these altitudes, only high-altitude cirrus clouds are present.

With these points established, it is now possible to estimate the impact of clouds on terrascope rays. It is stressed that the following is an approximate estimate and more detailed cloud modeling would be encouraged in future work to refine the estimate made here. The purpose of this section is to merely gauge the approximate feasibility of a terrascope when including clouds.

If one assumes a terrascope detector orbiting in Earth's equatorial plane, then lensed rays will be described by a great circle of constant longitude (or really one constant longitude

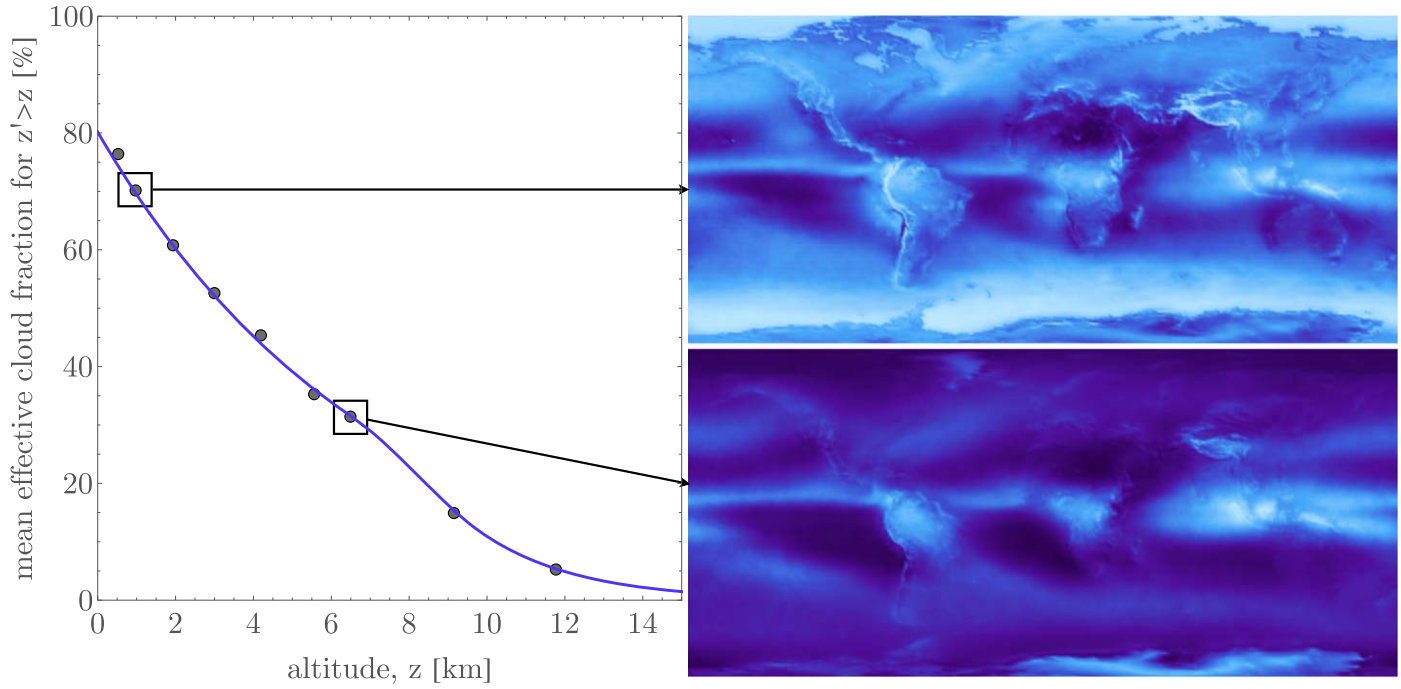

Figure 12. Left: effective cloud fraction, $N\epsilon$, averaged over all months and locations as measured over 11 yrs by HIRS, as a function of altitude (Wylie et al. 1994a, 1994b). Right: two example cloud maps from the data plotted on the left. Note how high-altitude clouds are much more common around the equatorial regions. (A color version of this figure is available in the online journal.)

plus another offset by 180°). Because the HIRS public data used here has a resolution of 1°, one can draw 180 such great circles—representing different rotational phases of the Earth. Working in the equatorial plane is not only a simplifying assumption but also minimizes the impact of high-altitude clouds which are more frequent at equatorial regions (see Figure 12).

For each great circle, there are 360 different locations (spread across latitude) sampled in the (interpolated) HIRS data. Because a terrascope detector located at $L = R_{\rm Hill}/2$ has focused red rays which traverse a depth of $(D - R) = 8.229$ km, at each location one can evaluate the cumulative effective cloud fraction above this altitude using the broken power law described earlier. Effective cloud fraction is not equal to cloud frequency. Fortunately, for high-altitude clouds (>6 km), the approximate relationship $N \simeq \frac{1}{2}N\epsilon$ may be used (Wylie et al. 1994a). Thus, at each of the 360 points along the great circle, the cloud frequency for all clouds above 8.2 km altitude can be estimated.

Because the cumulative fraction is defined as all altitudes above altitude z, and a terrascope ray indeed is forced to pass through all altitudes above z, the cloud frequency N may be interpreted as a time-averaged transmission fraction for the depth $(D - R)$. The total transmission can now be estimated by simply averaging over all such values along the great circle.

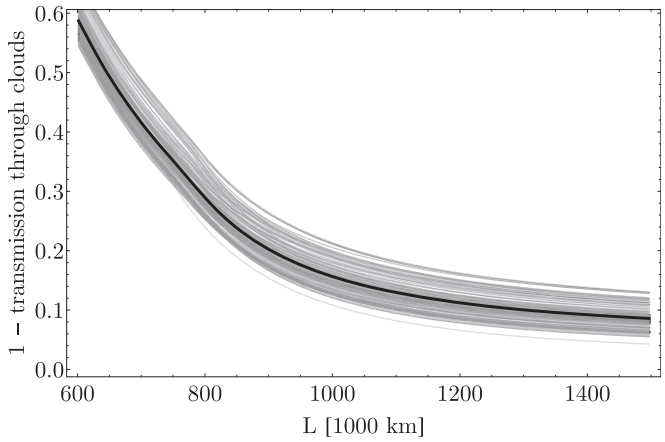

Figure 13. Estimated transmission through Earth's atmosphere due to clouds for a terrascope detector at a distance L. At one Hill radius (1,500,000 km), lensed rays travel no deeper than 13.7 km and thus largely avoid clouds, thereby losing less than 10% of the lensed light.

The results of this calculation are shown in Figure 13. A clear exponential trend is apparent in the results, highlighting as expected how more distant terrascope observatories are less affected by clouds. For the lowest $(D - R)$ allowed by our model, of 6 km, $L = 600{,}000$ km and the average cloud transmission is 41.4%. Moving out to $R_{\rm Hill}/2$, the situation is decidedly better with an average transmission of 64.9% and by

the time $L = R_{\rm Hill}$, 91.9% of the lensed rays make it through the atmosphere unimpeded by clouds. In conjunction with the earlier extinction calculations, these results strongly suggest that a terrascope detector as close to $L = R_{\rm Hill}$ as possible would optimize the setup.

4.5. Off-axis Lensing

Off-axis lensing was calculated using the method described in Section 3.5. The terrascope detector is fixed to a distance of $L = R_{\rm Hill}$ and to $W = 1$ m in what follows. The shape of the lensed source around Earth was computed for the US Standard Atmosphere 1976 model at various off-axis distances ranging from $Q = 0$ km to $Q = 40{,}000$ to 1000 km steps. As with the images shown in Figure 8, the rings are often egg-shaped (see Figure 14) and thus the area was calculated through numerically integration along 2000 uniformly spaced choices of ϕ, yielding an amplification value. The calculation was then repeated across the same grid of wavelengths used earlier in Section 3.1.

The amplification computed above describes the idealized case with no extinction. Because the shape is saved in each simulation, this information can be used to estimate the fraction of lost light due to clear-sky extinction and also that of clouds, using the same methods described earlier in Sections 4.3 and 4.4. Because the depth varies as a function of ϕ along the ring, the overall transmission is given by the amplification multiplied by the mean of the extinction over all 2000 phase points (where extinction here includes both the clear sky and cloud components). The resulting amplifications from this process are shown in Figure 14.

For offsets of $Q > 18{,}900$ km, the amplification has dropped to less than half that as on-axis. This may be converted into a timescale by nothing that at one Hill radius, a satellite would have a tangential velocity of $\simeq 0.5$ km s^{-1}. Accordingly, the lensing timescale would be $\sim$20 hr including both sides of the off-axis lensing, or roughly a day. During this time, the target has moved by approximately $1\overset{\circ}{.}4$ on the sky.

5. Discussion

5.1. Magnification

The calculations described thus far concern the amplification in flux of a distant source with a terrascope, but not the magnification in angular size of a source. Variations in Earth's atmosphere already present a major limiting factor in the resolving power of ground-based telescope and thus one should expect it to be an even greater for the terrascope. Even a Hill sphere observatory, exploiting stratospheric lensing, will observe rays that have traversed through $\sim$20 airmasses (see Figure 4) and thus seeing will be of order tens of arcseconds.

Consider a distant object whose light arrives at the Earth such that the object subtends an angle φ. This light is refracted and arrives at the terrascope detector subtending an angle $\theta = \Delta + \varphi$, where Δ is the deflection angle. The magnification is $\theta/\varphi = (\Delta/\theta - 1)^{-1}$. Since $\theta \simeq b/L$ and $\Delta = \Delta_0 e^{-(b-R)/H_\Delta}$, then magnification is approximately $[(\Delta_0 L/b)e^{-(b-R)/{\rm H}_\Delta} - 1]^{-1}$. Magnification thus theoretically tends to infinity, representing a caustic, as b approaches the value for maximum amplification. This caustic behavior not surprisingly echoes the situation of gravitational lensing, although practically realizing this magnification would not possible given the atmospheric disturbance.

5.2. Separation of Nearby Sources

The fact that an off-axis source still produces significant lensing as much as $1\overset{\circ}{.}4$ is useful, because lensing events occur over a prolonged timescale, but also potentially problematic. This is because it indicates that nearby sources, within a degree, will have some fraction of their light also lensed onto the detector and thus might be concerned about blending.

Consider the on-axis lensing scenario but with an additional source offset by an angle θ on the sky. The line connecting the contaminating source and the detector does not pass through the Earth's center (as with on-axis lensing) but rather is offset by a distance Q, meaning that $\theta = Q/L$. The on-axis lensed sourced travels through Earth's atmosphere at an impact parameter of $b_{\rm mid}$, which is equivalent to $\lim_{Q\to 0} b_{\rm mid}(Q)$, whereas the offset source has $b_{\rm mid}(Q)$. These two lensed images appear separated in the atmosphere, as seen from the detector, by an angle of α given by

$$\alpha = \frac{(\lim_{Q\to 0} b_{\rm mid}(Q)) - b_{\rm mid}(Q)}{L} \tag{39}$$

Accordingly, the apparent angular separation decreases from θ to α by the ratio

$$\frac{\alpha}{\theta} = \frac{(\lim_{Q\to 0} b_{\rm mid}(Q)) - b_{\rm mid}(Q)}{Q}. \tag{40}$$

Using the numerical results from Section 4.5, this ratio can be computed for any given wavelength and at any given phase angle around Earth. For $Q > 20{,}000$ km, all phase angles converge to a $\frac{\alpha}{\theta}$ ratio of one over a few thousand, because the detector has a diffraction limited angular resolution of $1.22\frac{\lambda}{W}$, then the source separation ability of the terrascope will be $\sim\frac{\lambda H_\Delta}{WR}$. This is $\simeq 0.25$ milliarcseconds for a 1 metre detector at 1 μm and thus is a factor of $1.22H_\Delta/W$ improved.

Aside from resolving a contaminant through angular separation, it may be possible to separate sources (to some degree) based on the distinct temporal lensing light curves that emerge due to the differing geometries.

5.3. Atmospheric Radiance

Earth's atmosphere is luminous from airglow, scattering, and thermal emission and this radiance poses an obstacle to the

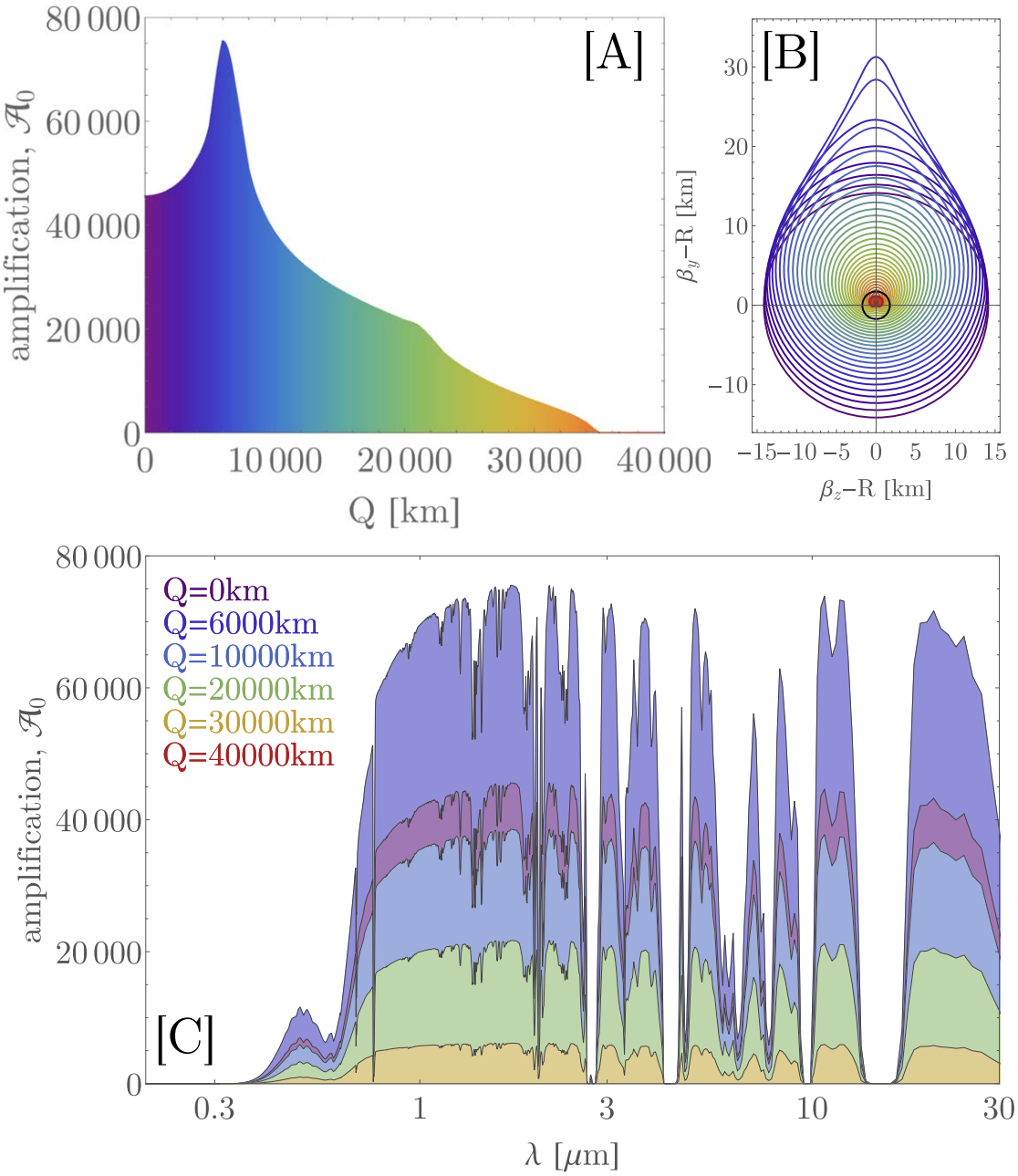

Figure 14. Off-axis lensing through the terrascope. Panel (A) shows the amplification after extinction for $\lambda = 1.74$ μm. Panel (B) shows the simulated lensed images for 41 evenly spaced offset distances from $Q = 0$ km to $Q = 40{,}000$ km. Panel (C) shows the spectral amplification at six different offset distances.

terrascope. By using a shade adapted for Earth, it may be possible to remove flux from Earth's disk, which greatly outshines the sky brightness. A simple shade would need to be offset from the detector by a distance of $L[b/(W + b)]$ in order to occult the Earth's disk and have a radius of $R[W/(W + b)]$. For all detectors with $W < 0.209$ m (corresponding to an effective telescope diameter of 96.9 m), the effective collecting area of the terrascope exceeds the size of the Earth-shade. It may be still economical to go beyond 0.2 m since the cost of a shade is expected to be cheaper than a mirror.

Scattering from the upper atmosphere will be ever present, and represents a source of background (rather than necessarily a source of noise). This background will be strongly dependent upon the relative position of the Sun during the

observations. Let us denote the angle subtended from Earth to the terrascope detector to the Sun as Θ. If $0^\circ < \Theta < 90^\circ$ or $270^\circ < \Theta < 360^\circ$, then the Sun will appear directly in view to the detector excluding observations during this time. If $90^\circ{+}18^\circ < \Theta < 270^\circ{-}18^\circ$, then one side of Earth will be in astronomical twilight where scattered sunlight cannot interfere (except at the instant of $\Theta = \pi$). If the observatory is exactly in the ecliptic plane, then at any one time during this range in Θ exactly one half of Earth's circumference will be in astronomical twilight.

Accordingly, it is estimated here that the actual amplification from a terrascope will be one half of that depicted in the various figures throughout. This assumes that any part of Earth which is illuminated will have a background component that is simply not removable. However, more detailed calculations than possible here may be able demonstrate that at least some fraction of this lost capability can be recovered through background suppression strategies, such as leveraging polarization, wavelength information, and temporal light-curve variations. These are undoubtedly technical challenges for a realized terrascope but effort should be encouraged to explore overcoming them given the very large gains potentially given by such a system.

5.4. Atmospheric Stability

The refractivity of air at a specific altitude will vary as a function of position and time in a realistic atmosphere. It is argued here that so long as the terrascope detector is a significant distance away from the inner focal point, these variations will not affect the amplification factor in a meaningful way. Consider a particular location where there is a increase in pressure at altitude z compared with the typical pressure at altitude z. This causes the refractivity to increase and thus light traveling at that location will now refract too much and miss the detector at distance L. However, there must be an altitude $z' > z$ where the pressure decreases back down to the typical pressure, thereby refracting light back onto the detector. In this way, the perfect circular ring image is distorted into an irregular ring, but the thickness of the ring is the same and thus the amplification is unchanged.

5.5. Pointing

Because an off-axis source still causes significant lensing at $1\overset{\circ}{.}4$ for a Hill sphere terrascope, this denotes the approximate angular band on the sky suitable for observation. This represents just under one percent of the sky. The orbital plane of the detector is a free parameter but ecliptic observing minimizes the affect of high-altitude clouds and solar scattering, as well as providing the densest field of targets. Pointing is naturally limited to whatever happens to be behind Earth at any given time, although fleets of terrascope detectors could increase the coverage as needed.

5.6. Radio Terrascope

The calculations of extinction in this work strictly assume optical/infrared light. Moving further out into the radio offers two major advantages though. First, extinction due to clouds can be largely ignored, allowing for detectors much closer including on the lunar surface. Second, solar scattering is far less problematic in the radio and indeed it is typical for radio telescopes to operate during daylight phases. The simple refraction model of this work was extended to the radio and indeed the amplification was estimated to be largely achromatic beyond a micron. Nevertheless, the model did not correctly account for the radio refractivity as a function of humidity, nor the impact of the ionosphere on lensed rays. Accordingly, a radio terrascope may be an excellent topic for further investigation. It should be noted though that a disadvantage of a giant radio receiver in space is that humanity already regularly builds large receivers on Earth at much lower expense than their optical counterparts. Thus, the benefit of going into space for radio observations may not prove ultimately economical.

D.M.K. is supported by the Alfred P. Sloan Foundation. Thanks to members of the Cool Worlds Lab and the NASA Goddard Institute for Space Science group for useful discussions in preparing this manuscript. Thanks to Jules Halpern, Duncan Forgan, Caleb Scharf, and Claudio Maccone for reviewing early drafts and discussions of this work. Special thanks to Tiffany Jansen for her assistance with coding questions. Finally, we thank the anonymous reviewer for the constructive feedback.

Software: `lowtran7`(Kneizys et al. 1988).

References

Birch, K. P., & Downs, M. J. 1994, Metro, 31, 315
Cassini, J. D. 1740, Tables astronomiques, 34
Eddington, A. S. 1919, Obs, 42, 119
Edlén, B. 1994, Metro, 2, 71
Einstein, A. 1916, AnP, 49, 769
Elvis, M. 2016, Frontier Research in Astrophysics II, arXiv:1609.09428
Heidmann, J., & Maccone, C. 1994, AcAau, 32, 409
Kneizys, F. X., Shettle, E. P., Abreu, L. W., et al. 1988, Air Force Geophysics Lab, Tech. Rep., AFGL-TR- 88-0177
Kraus, J. D. 1986, Radio Astronomy (Powell: Cygnus-Quasar Books), 6
Michael, S. L. 1999, Statistical Interpolation of Spatial Data: Some Theory for Kriging (New York: Springer)
Monnier, J. D. 2003, RPPh, 66, 789
National Geophysical Data Center 1992, P&SS, 40, 553
Rasmussen, C. E., & Williams, C. 2006, Gaussian Processes for Machine Learning (Cambridge, MA: MIT Press)
Turyshev, S. G., & Andersson, B.-G. 2003, MNRAS, 341, 577
van Belle, G. T., Meinel, A. B., & Meinel, M. P. 2004, Proc. SPIE, 5489, 563
von Eshleman, R. 1979, Sci, 205, 1133
Wylie, D. P., Menzel, P. W., & Strabala, K. I. 1994a, JCli, 12, 170
Wylie, D. P., Menzel, P. W., Woolf, H. M., & Strabala, K. I. 1994b, JCli, 31, 1972